One-step green synthesis of platinum mesoporous nanoparticles by riboflavin for light activated antitumoral therapy

Raquel Rey-Méndez [a], Noelia González-Ballesteros [a], María C. Rodríguez-Argüelles [a,*], Silvana Pinelli [b], Paola Mozzoni [b,c], Benedetta Ghezzi [b,d,e], Francesca Rossi [e], Filippo Fabbri [f], Giancarlo Salviati [e], Franca Bigi [e,g]

[a] Dept. Química Inorgánica, Universidade de Vigo, 36210, Vigo, Spain
[b] Dept. of Medicine and Surgery, University of Parma, via Gramsci 14, 43126, Parma, Italy
[c] CERT, Centre of Excellence for Toxicological Research, University of Parma, via Gramsci 14, 43126, Parma, Italy
[d] Centre of Dental Medicine, University of Parma, via Gramsci 14, 43126, Parma, Italy
[e] IMEM-CNR Institute, Parco Area delle Scienze 37/A, 43124, Parma, Italy
[f] NEST, Istituto Nanoscienze – CNR, Scuola Normale Superiore, Piazza San Silvestro 12, 56127, Pisa, Italy
[g] Dept. SCVSA, Universiy of Parma, Parco Area delle Scienze 17/A, 43124, Parma, Italy

ARTICLE INFO

ABSTRACT

Photodynamic therapy (PDT) has been established as one of the most promising novel cancer therapies with fewer side-effects and enhanced efficacy compared to the currently available conventional treatments. However, its application has been hindered by the limitations that photosensitizers (PS) have. The combination of PS with metallic nanoparticles like platinum nanoparticles (PtNPs), can help to overcome these intrinsic drawbacks. In this work, the combination of PtNPs and the natural photosensitizer riboflavin (RF) is proposed. PtNPs are synthesized using RF (Pt@RF) as reducing and stabilizing agent in a one-step method, obtaining nanoparticles with mesoporous structure for UV triggered PDT. In view of possible future UV irradiation treatments, the degradation products of RF, ribitol (RB) and lumichrome (LC), this last being a photosensitizing byproduct, are also employed for the synthesis of porous PtNPs, obtaining Pt@LC and Pt@RB. When administered in vitro to lung cancer cells, all the samples elicit a strong decrease of cell viability and a decrease of intracellular ATP levels. The antitumoral effect of both Pt@RF and Pt@LC is triggered by UV-A irradiation. This antitumoral activity is caused by the induction of oxidative stress, shown in our study by the decrease in intracellular glutathione and increased expression of antioxidant enzymes.

1. Introduction

The research of alternative treatments for aggressive and untreatable cancer types is of primary importance. Light triggered therapies, such as photodynamic therapy (PDT), have shown in several clinical studies improvements in the tumor specificity of photosensitizers thanks to targeting or localized activation, and fewer side-effects compared to conventional treatments [1]. The therapeutic efficacy of PDT derives from the ability of a photosensitizing molecule (PS) to produce cytotoxic singlet oxygen and/or other reactive oxygen species (ROS) upon activation by light irradiation, e.g. infrared (IR) or ultraviolet (UV), to induce cell death [2]. Its clinical application, however, has encountered some limitations, such as low PS bioavailability. This limitation could be overcome by formulating novel PDT agents consisting in a natural PS conjugated to a metal nanoparticle [3]. The use of these nanostructures improves the bioavailability and enhances the therapeutic efficacy by synergy with other cell death mechanisms, like e.g. the case of riboflavin photoproducts that can provide potential candidates for improving the efficiency of melanoma treatment [4]. Another limitation is the inefficient light penetration in the tissues. In particular, UV excited PDT is vastly employed in dermatology for treating skin cancer [5]. However, recently, with the development of UV enhanced optical fiber, this particular therapy can also be employed in intra-operative treatment, or it can locally treat a tumor mass inside the body using a fiberscope [6]. The use of optical fibers has been employed clinically for the treatment of deep-seated tumors such as prostate, pancreas, head, neck and even brain

[7]. Moreover, lung cancer can also be treated with this technology thanks to the use of lasers delivered by flexible diffuse fibers through bronchoscopy [8].

Riboflavin (RF), known as vitamin B2, is also an efficient photosensitizer that matches the requirements for a good PDT agent [9]. By photoirradiation, RF excites to its triplet state (^{3}RF*), with a quantum yield of 0.6. This species is a very strong oxidating agent (^{3}RF*/RF = 1.62 V). RF can operate, as most photosensitizers, by two mechanisms: either by mediating the direct oxidation of biomolecules (Type I), generating ROS, or by transferring excitation energy to molecular oxygen (Type II), generating singlet oxygen [10].

The efficacy of RF alone for PDT has been tested in several different cell lines [11,12]. RF conjugated with pectin-coated AgNP was analyzed in HeLa incubated cells [13]. With this conjugate, the yield of RF triplet state is increased, therefore increasing the amount of ROS generated. The presence of AgNP is, thus, beneficial for the improvement of RF-mediated PDT.

RF is also photo and thermo sensitive, therefore getting decomposed by several pathways that, depending on the conditions (pH, buffer kind and concentration, light intensity and wavelength, viscosity and polarity of solvent, metal ion complexation and ionic strength), can lead to several different products following different mechanisms [14–16]. The main product in the photothermal degradation is lumichrome (LC), that results from the cleavage in acid media of the RF side chain, and ribitol (RB) [17].

LC is also known as a photosensitizer, that is able to generate singlet oxygen [18]. It is known to have a role in some biological functions and its anticancer effect was also highlighted without radiation [19,20]. However, so far, no studies have been published that address what effect the UV radiation could have in the anticancer properties of this molecule.

RB is an acyclic sugar polyalcohol. It does not have neither UV–Vis absorption nor emission properties and, therefore, it does not share the photosensitizing properties that RF and LC have. However, it does possess some anticancer activity. Its potential application as a therapeutic agent in combination with other treatments has been tested in different cancer cell lines, finding good results for breast cancer (MCF7 cells) [21, 22].

With regard to combination with metal nanoparticles, platinum nanoparticles (PtNPs) are a good candidate. The study of PtNPs has recently been broaden, owing to their wide range of applications, from catalysis, to biosensing, electroanalysis and biological applications [23]. Regarding cancer therapy, they were shown to possess some intrinsic cytotoxic activity [24], good biocompatibility [25] and great photothermal properties, being able to elicit cell death under laser light activation [26,27]. Another key advantage of PtNPs is the wide variety of structures that can be engineered and that exhibit different properties [28]. In this regard, mesoporous platinum structures have recently been developed. These structures possess abundant pores, therefore offering a larger superficial area that can be used for surface modification with different molecules and therapeutic agents. In the last few years, PtNPs mesoporous structures have been combined with well-known anticancer drugs and their efficacy has been tested in cancer cell lines (e.g., melanoma, breast cancer …) [26,27,29–31]. However, to the best of our knowledge, this combination of mesoporous PtNPs with natural photosensitizers for PDT has not been tested yet.

In this work, we present the one-step synthesis of mesoporous PtNPs with riboflavin acting as reducing and stabilizing agent. In addition, we analyzed the photo-chemical properties of the Pt@RF in the perspective of the application in photodynamic therapy excited by UV light. We also investigated the ability of RF degradation products, namely lumichrome and ribitol, to promote the synthesis of platinum nanoparticles and we evaluate their possible photosensitizing properties. The anticancer activity of these different nanostructures was evaluated in vitro, against lung cancer cells. When illuminated by UV light, Pt@RF and Pt@LC prove to be highly effective, allowing to dramatically (−70 % at 24 h, −80 % at 48 h) reduce the cell viability, while the Pt@RB does not present any photosensitizing activity.

2. Experimental section

2.1. Materials

Riboflavin, 98 % was purchased from Alfa Aeasar. Lumichrome and ribitol, ≥99 % were purchased from Sigma-Aldrich. Platinum (IV) chloride 99 % was purchased from Acros Organics. Trisodium citrate dihydrate and L-ascorbic acid were purchased from AnalaR NORMAPUR. Sodium borohydride and sodium hydroxide pellets were purchase from Merck and Panreac respectively. The reagents were employed in analytical grade and without further purification in the assays. Milli-Q water was used in all the experiments.

CellTiter-Glo luminescent assay and GSH/GSSG-GloTM assay were purchased from Promega Madison (WI, USA). 3-(4,5-dimetiltiazol-2-il)-2,5-difeniltetrazolio bromuro (MTT), bovine serum albumin and 3 % normal goat serum were purchased from Sigma-Aldrich. TRIzol and DNase I were purchased from Thermo Fisher(CA, USA). TRITC-conjugated phalloidin primary antibody (cat. 90228) and DAPI (cat. 90229) were purchased from Merk Millipore (Darmstadt,DE).

2.2. Synthesis of platinum nanoparticles

Riboflavin (RF), lumichrome (LC), and ribitol (RB) were employed for the synthesis of platinum nanoparticles (Pt@RF, Pt@LC, Pt@RB, respectively). In all the cases, several reaction conditions were tested, modifying the concentration of RF, LC and RB and the concentration of platinum salt, the temperature and reaction time. All the reactions were monitored by color change and UV–Vis spectroscopy.

The optimal synthesis was obtained by heating to 90 °C with constant stirring an aqueous solution of each organic compound - adding either 1.25 mL of 0.13 mM aqueous RF, 0.7 mL of 0.2 mM aqueous LC, or 15 μL of 10 mM aqueous RB, in a final volume of 5 mL of water - to obtain a final concentration of 0.03 mM. When this temperature was reached, 100 μL of 10 mM aqueous PtCl$_4$ was added in all the cases, to obtain a final concentration of 0.2 mM of PtCl$_4$. This mixture was left at 90 °C with constant stirring, protected from light, and it was monitored by UV–Vis spectroscopy until no more changes were observed. The process lasted 7 h for Pt@LC and 24 h for Pt@RF and Pt@RB. Bare platinum nanoparticles (PtNPs) were also prepared by following a slightly modified version of Sidker et al. procedure to obtain the same platinum concentration as in Pt@RF, Pt@LC and Pt@RB [32].

2.3. Characterization techniques

UV–Vis spectra were acquired at room temperature on a Jasco Spectrometer V-670. Fluorescence spectra were acquired at room temperature on a Jasco FP-8600 NIR Spectrofluorometer. Transmission Electron Microscopy (TEM) analysis was performed on samples prepared by drop casting the nanoparticles dispersion directly onto a holey carbon film supported on a copper grid. To obtain better quality images, it was necessary to centrifuge the samples at 10000 rpm for 60 min to eliminate the excess of organic material. Conventional images were acquired with a JEOL JEM1010 microscope operated at 100 kV, while High Resolution Transmission Electron Microscopy (HRTEM) and Scanning Transmission Electron Microscopy (STEM) images were acquired with a JEOL JEM2010F field emission gun microscope, operated at 200 kV. Coupling between the STEM unit and the Energy Dispersive X-ray (EDX) detector (Oxford Inca Energy 200) was used to obtain elemental maps. Data collection and analysis were carried out using Digital Micrograph software by Gatan.

Zeta-potential measurements were obtained through electrophoretic mobility by taking the average of five measurements at the stationary level using a ZetasizerNano S (Malvern Instruments, Malvern U.K.) equipped with 4 mW He–Ne laser, operating at a wavelength of 633 nm.

The solutions were measured as they were obtained in the reaction, without any purification procedures.

A PerkinElmer Optima-4300 DV ICP-OES (PerkinElmer, Waltham, Massachusetts, USA) was used for the determination of the platinum concentration using indium as an internal standard. For the preparation of the samples, a 24 h digestion with aqua regia was performed.

High Performance Liquid Chromatography coupled with Tandem Mass Spectrometry (HPLC-MS/MS) technique was performed using Agilent Technologies 1260 chromatographer coupled with a SCIEX Tri-ple Quad 3500 detector. The sample was obtained by centrifugation of the nanoparticle solution at 10000 rpm for 1 h and separating the su-pernatant from the pellet. This supernatant was directly measured without dilution.

Fourier Transformed Infrared Spectroscopy (FTIR) experiments were measured with Jasco FT/IR-6100 spectrophotometer at a resolution of 4 cm^{-1} in the range of 4000–400 cm^{-1}. The commercial riboflavin, lumi-chrome and ribitol solids were grounded to fine powder and used to record the spectra employing KBr pellet technique. For the preparation of the other samples, the solutions were dried in an oven for 24 h at 100 °C.

Raman spectroscopy was carried out with a Renishaw InVia system, equipped with confocal microscope, a 785 nm excitation laser and a 1200 line/mm grating (spectral resolution <3 cm^{-1}). All the analyses were performed with a 50x long working distance objective (NA = 0.55).

2.4. Biological assays

2.4.1. Cell culture and treatments

A549 alveolar basal epithelial cells were cultured to achieve expo-nential grow in RPMI 1640 medium supplemented with 10 % heat-inactivated FBS, 100 U penicillin mL^{-1}, 100 μg streptomycin mL^{-1}, and 2 μM L-glutamine, then incubated at 37 °C with humidified air containing 5 % CO_2.

Cells were seeded into 96-well plates to a concentration of $1x10^5$ cell/ mL, incubated for 24 h and then treated with samples. The samples were previously suspended in ultra-pure water at the concentration of 1 mg/ mL, sonicated immediately before use for 30 min at 50 W (50/60 Hz) using a bath sonicator (Transsonic T460 Elma Ultrasonic, Singen, Ger-many) and diluted in culture medium to the final working concentrations.

To study the effects of light activation, cells in half of the wells were irradiated for 2 h using a commercial Wood lamp (power 25 Watt) emitting UV-A light with a spectrum centered at 375 nm.

2.4.2. Cell viability

A549 cell viability, after 24 or 48 h from treatment, was determined by CellTiter-Glo Luminescent Assay, following the manufacturer's in-structions. Luminescence was detected by a Varioskan™ LUX Multimode Microplate Reader (Thermo Fisher Scientific™, Walthan, NE, USA) and the data were normalized against control (untreated cells). To confirm these data, we performed the MTT test (3-(4,5-dimethylthiazole)-2, 5-diphenyltetrazoliumbromide). MTT reagent was added into each well and incubated at 37 °C for 3 h. Reaction was stopped by adding 100 μL solubilization solution and the absorbance was detected with the microplate reader at a wavelength of 560 nm. Viable cells (impermeable to Trypan Blue) were further counted in a hemocytometer.

2.4.3. Cellular uptake

Cell morphology was monitored with an inverted microscope (Olympus CK40-RFL, Tokyo, Japan). Cells treated with Pt@RF were selected for the analysis of the nanoparticles cellular uptake by confocal microscopy, in a Stellaris 5 (Leica, Wetzlar, Germany) microscope, exploiting the riboflavin fluorescence. Cells were seeded on a glass slide at a density of 20000 cells/spot, incubated for 24 h and treated with 300 μg/mL of Pt@RF. After 24 h from the treatment, the slides were washed in PBS and fixed in 4 % p-formaldehyde. Subsequently, specific antigenic sites were blocked with 10 % bovine serum albumin and 3 % normal goat

serum for 90 min. Then, slides were incubated for 60 min with TRITC-conjugated phalloidin primary antibody at a dilution of 1:100. After that, slides were washed twice with PBS and stained with DAPI for nuclei detection. Samples were observed at the confocal microscope with an oil immersion objective 63×, setting the excitation/emission wavelength to 358/460 nm, 488/520 nm and 630/680 nm for the acquisition of the blue (nuclei), green (Pt@RF) and red (cytoplasm) components, respec-tively. Z-stacks were acquired with a step size of 2 μm.

2.4.4. Oxidative stress

Glutathione (GSH and GSSG) levels were determined by GSH/GSSG-Glo™ Assay, in accordance with the manufacturer's protocol. Lumines-cence was detected by a Varioskan LUX Multimode Microplate Reader (Thermo Fisher Scientific, Walthan, NE, USA). The values were normal-ized to cell numbers and expressed as percentages of the controls.

2.4.5. RNA extraction and gene expressions

Total RNA was extracted from 10^5 cells using commercially available TRIzol and digested with DNase I to remove any genomic DNA contamination. Total RNA was quantified using a Varioskan LUX spec-trophotometer (Thermo Fisher Scientific, Walthan, NE, USA). cDNA was synthesized using a commercial kit based on the use of inverse tran-scriptase (Thermo Fisher Scientific, Walthan, NE, USA). Then it was amplified by means of real-time PCR (RT-PCR) using specific primers including exon-exon junctions specifically designed for heme oxygenase 1 (HO-1), superoxide dismutase 1 (SOD1) and 2 (SOD2). The expression values were normalized to expression of ribosomal protein L13 (RPL13) housekeeping gene. The changes in expression of each mRNA respect to untreated controls were calculated using equation $2^{-\Delta\Delta Ct}$.

2.4.6. Statistical analysis

SPSS software version 28 (SPSS Inc/IBM, Chicago, Ill, USA) was used for analysis. Data of at least three independent experiments are pre-sented, as mean ± standard deviation. All groups were analyzed using two-way ANOVA followed by Bonferroni post-hoc test. Statistical sig-nificance was set at $p < 0.05$ (two-sided).

3. Results and discussion

3.1. Synthesis and characterization of platinum nanoparticles

3.1.1. Synthesis of platinum nanoparticles with RF, LC and RB

Riboflavin was initially selected as natural photosensitizer for the nanoparticles synthesis. To find the best conditions for the synthesis, different parameters were tested using RF as the reducing agent. The influence of reducing agent concentration was tested in a range of con-centrations from [RF] = 0.12 to 0.01 mM. The highest and lowest con-centrations employed resulted in a not optimal particle formation, leading to the precipitation of large aggregates, as it can be seen by the UV–Vis spectra (Figure S1 a), that do not show the typical surface plas-mon resonance (SPR) band that would correspond to PtNPs. It is known from previous works that the presence of both too high and too low concentrations of reducing agents favors the aggregation of platinum nanoparticles [33]. The effect of platinum concentration was also tested in a range from 0.6 to 0.2 mM. A shift to longer wavelengths of the SPR band of PtNPs was observed as the platinum concentration increased (Figure S1 b). The effect of the temperature was also tested heating at 30, 70 and 90 °C. The UV–Vis spectra showed that there is a narrowing of the SPR band as the temperature increased (Figure S1 c), therefore TEM images were acquired to observe how these changes affected the morphology of the PtNPs synthesized. Fig. S2 shows that at 30 °C poorly defined clusters were formed, together with dispersed smaller nano-particles. At 70 °C, the formation of bigger nanoparticles with a mean diameter size of 28 ± 5 nm was observed. Finally, the synthesis at 90 °C led to the formation of spherical more homogeneous nanoparticles with a mean diameter size of 37 ± 4 nm. These results are in agreement with

other studies that have stablished that higher temperatures favor the formation of larger PtNPs [34,35].

As detailed in the experimental section, the best combination of the parameters was 0.03 mM of RF and 0.2 mM of PtCl$_4$, at 90 °C for 24 h. Since the synthesis of Pt@RF is carried out at high temperature and the pH of the solution is slightly acid, the issue of thermal stability of RF arises. Several previous studies [36,37], indicate that RF undergoes degradation when aqueous solution of this molecule is heated in a range of temperatures, observing a direct relationship between temperature increase and degradation, being the main degradation product in acid media lumichrome (LC) (Scheme S1). The possible degradation of RF during the synthesis of Pt@RF was studied, by analyzing the supernatant resulting after centrifugation of Pt@RF by HPLC-MS/MS and using standard solutions of RF, RB and LC of known concentrations as reference. The concentration of the three species in the solution can be seen in Table 1.

Published studies suggest that the proportion of molecules of RF that undergo degradation are in the range of 4–28 %, which is consistent with the results obtained in our assay, although there is a high dependency of this percentage on the concentration and temperature [36]. The cited study was carried out in free RF aqueous solution and no studies of RF degradation in presence of PtNPs have been found.

Therefore, for a more complete study, the synthesis of PtNPs was also attempted using LC and RB. For better comparison, the conditions chosen were the same of those used with RF, that is: a concentration of 0.2 mM of aqueous PtCl$_4$ added to a concentration 0.03 mM of aqueous LC or aqueous RB solution, at 90 °C. The reaction lasted 7 h for the synthesis of Pt@LC and 24 h for the synthesis of Pt@RB.

Finally, for means of comparison, PtNP were synthesized without any photosensitizer using a classical chemical method as described in the experimental section [32]. Characterization confirmed the formation of 35.8 ± 5.2 nm porous PtNP with a SPR band in 293 nm (Fig. S3) while the FTIR spectra of PtNP is reported in Fig. S4.

3.1.2. Characterization of Pt@RF, Pt@LC and Pt@RB

A deeper optical and structural characterization of the nanoparticles obtained at the optimal conditions was performed. The UV–Vis spectrum of Pt@RF was recorded (Fig. 1 a) and compared to that of the free molecule. The main difference between the two spectra is that the characteristic bands of RF at 370 nm and 445 nm are not visible in the spectrum of Pt@RF, since there is a broad band with a maximum of absorption at 270 nm that is covering them. This band corresponds to the SPR band of PtNPs, that appears usually in the range of 250–300 nm as it has been reported earlier in the synthesis of other platinum nanoparticles [38–40]. This SPR band covers the spectrum of RF because PtCl$_4$ is in a much higher concentration in the reaction than RF. In the case of Pt@LC, the characteristic absorption bands of this molecule can be recognized, superimposed to the SPR band of PtNPs (Fig. 1b). In the case of RB, the molecule itself does not have any absorption so the only contribution in the spectrum of Pt@RB is the one corresponding to the PtNPs SPR at 260 nm (Fig. 1 c).

When the Pt@RF solution was excited at the optimal excitation wavelength of RF, the fluorescence emission of this molecule was identified by an emission band centered at 528 nm (Fig. 1 d). This emission is, however, severely quenched by the presence of PtNPs, compared to the natural emission of RF that exhibits an intense emission band at 530 nm. Previous works report the effect of fluorescence quenching of RF in the presence of other metals, probably due to energy transfer processes [14].

Table 1
Concentration and percentage of RF, LC and RB in the Pt@RF supernatant, determined by HPLC-MS/MS.

	RF	LC	RB
mg/L	10.60 ± 0.25	1.19 ± 0.05	0.34 ± 0.03
%	87.4	9.8	2.8

Pt@LC, just like in the case of Pt@RF, retained the natural wavelength emission of free-standing LC when the nanoparticle sample is excited at the optimal excitation wavelength of LC (Fig. 1 e). This emission is also slightly quenched by the presence of PtNPs.

Characterization of the size of Pt@RF by low-resolution TEM gave a mean metallic diameter of 37 ± 4 nm and a narrow distribution histogram (Fig. 2 a and b), made after measuring a statistically significant number of nanoparticles (>100). Low resolution TEM also indicated that the mean diameter size was 54 ± 8 nm for Pt@LC (Fig. 2 c and d) and of 42 ± 4 nm for Pt@RB (Fig. 2 e and f). The platinum nanoparticles synthesized with LC are the largest of the three, followed by Pt@RB and the smallest ones are the Pt@RF. The stability was confirmed by zeta potential measurements, that gave a value of −29.5 ± 2.3, −18.5 ± 1.4 and −25.1 ± 1.74 mV for Pt@RF, Pt@LC and Pt@RB respectively (Fig. S5). These values indicate that they all carry a negative surface charge [41].

High-resolution TEM (HRTEM) images revealed the porous structure of Pt@RF, Pt@LC and Pt@RB nanoparticles. All the nanoparticles are formed by smaller 2–3 nm primary nanoparticles that grow together forming nearly spherical structures (Fig. 3). Each one of these primary nanoparticles is a single crystal domain. The d-spacings were determined and the corresponding Miller indexes were assigned using tabulated data (JCPDS Card No 98-006-0819). Two different preferential d-spacings of 0.23 nm and 0.19 nm were measured, corresponding to the (111) and (200) planes respectively. These data are consistent with the face-centered cubic (FCC) structure of platinum [42]. The most probable growth mechanism for this type of nanoparticles is the occurrence of frequent coalescence events of smaller primary particles [43]. Through structural relaxation, the primary nanoparticles reorient their crystal structures. The places where the reorientation was not successful, give rise to defects that allow this type of nanoparticles to have higher energy surface sites. However, the structure of the nanoparticles is too complex to be determined by a single HRTEM image [44] and multiple growth mechanisms can take place simultaneously [45].

These porous PtNPs structures are known to be formed under mild reducing conditions [46]. RF, LC and RB act both as reducing and stabilizing agents in a one-step nanoparticle synthesis in each case. The presence of organic material attached to the surface of the porous nanoparticles was confirmed by EDX technique (Figs. S6 and S7 and S8). The EDX spectra showed the presence of Pt, C and O. The copper signals is owed to the grid used in the experiment. As it can be seen in the mixed elemental map, Pt is gathered in the nanoparticles, and it is covered by a coat of organic material. This organic material is surrounding the metallic nanoparticles. The concentration of 0.2 mM of Pt in the samples was confirmed by ICP-OES analysis of the Pt@RF, Pt@LC and Pt@RB solution after digestion with aqua regia.

Possible changes of the organic part due to the synthesis of the nanoparticles were assessed by FTIR spectroscopy, analyzing whether the vibrational modes of RF, LC and RB show any changes (Fig. 4 a, b and c). The bands in RF that corresponded to OH and NH vibrations at 3490, 3335 and 3208 cm^{-1} transform into a wider band centered at 3408 cm^{-1} [47]. The bands at 3034 and 2933 cm^{-1} in RF appear in 2961 and 2924 cm^{-1} in the spectrum of the Pt@RF and are probably due to CH, CH$_2$ and CH$_3$ vibrations [47]. The bands at 1730 and 1648 cm^{-1} correspond to C–O stretching in the spectrum of RF and these appear at 1703 and 1641 cm^{-1} in the spectrum of Pt@RF [48]. The bands at 1578 and 1542 cm^{-1} are assigned to N–C stretching vibrations of the aromatic rings, as well as the bands at 1396, 1344, 1299 and 1244 cm^{-1} and these remain unshifted in the Pt@RF spectrum [49,50]. In the case of Pt@LC (Fig. 4 b), the spectra share the broad band at 3408 cm^{-1}, that corresponds to OH vibrations. However, this band is much less intense in LC. This molecule has bands in 3184 and 3059 cm^{-1} that do not appear in the Pt@LC spectrum. These bands are attributed to N–H stretch; therefore, this could imply the oxidation of these functional groups [51]. In the case of Pt@RB (Fig. 4 c), the spectrum shows clear similarities with the spectrum of RB. However, there's a major difference: the appearance of a new band at 1633 cm^{-1} assigned to the presence of a C=O bond. This type of bond is
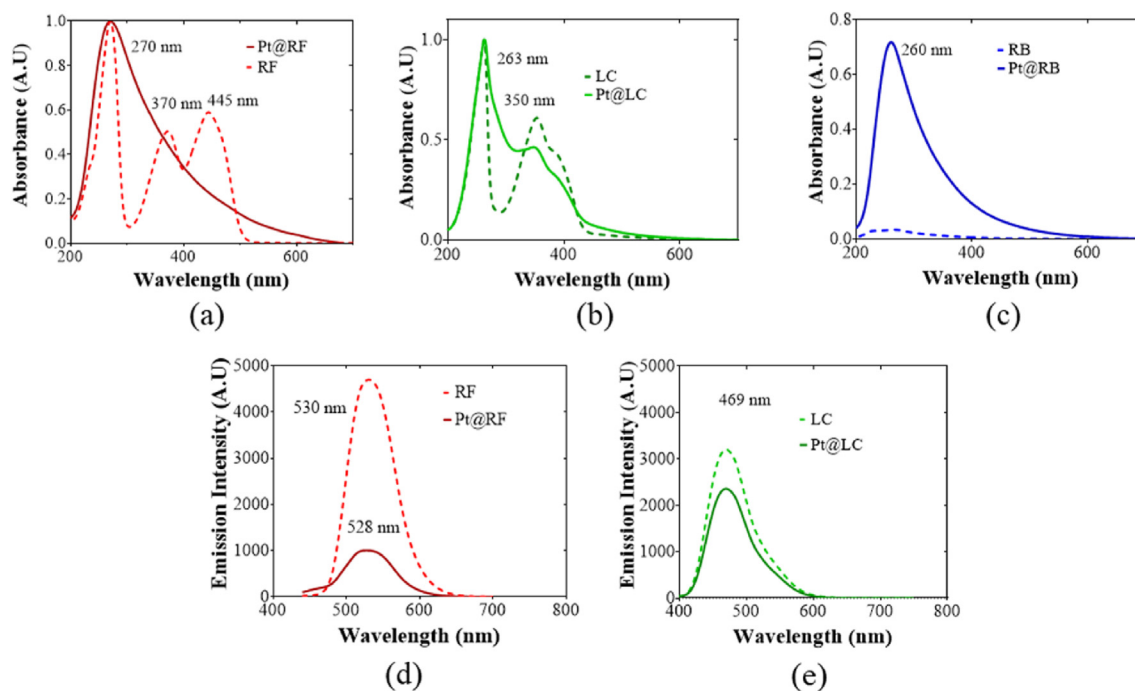
Fig. 1. UV–Vis spectra before and after the synthesis of (a) Pt@RF, (b) Pt@LC and (c) Pt@RB; Fluorescence spectra before and after the synthesis of (d) Pt@RF and (e) Pt@LC respectively.
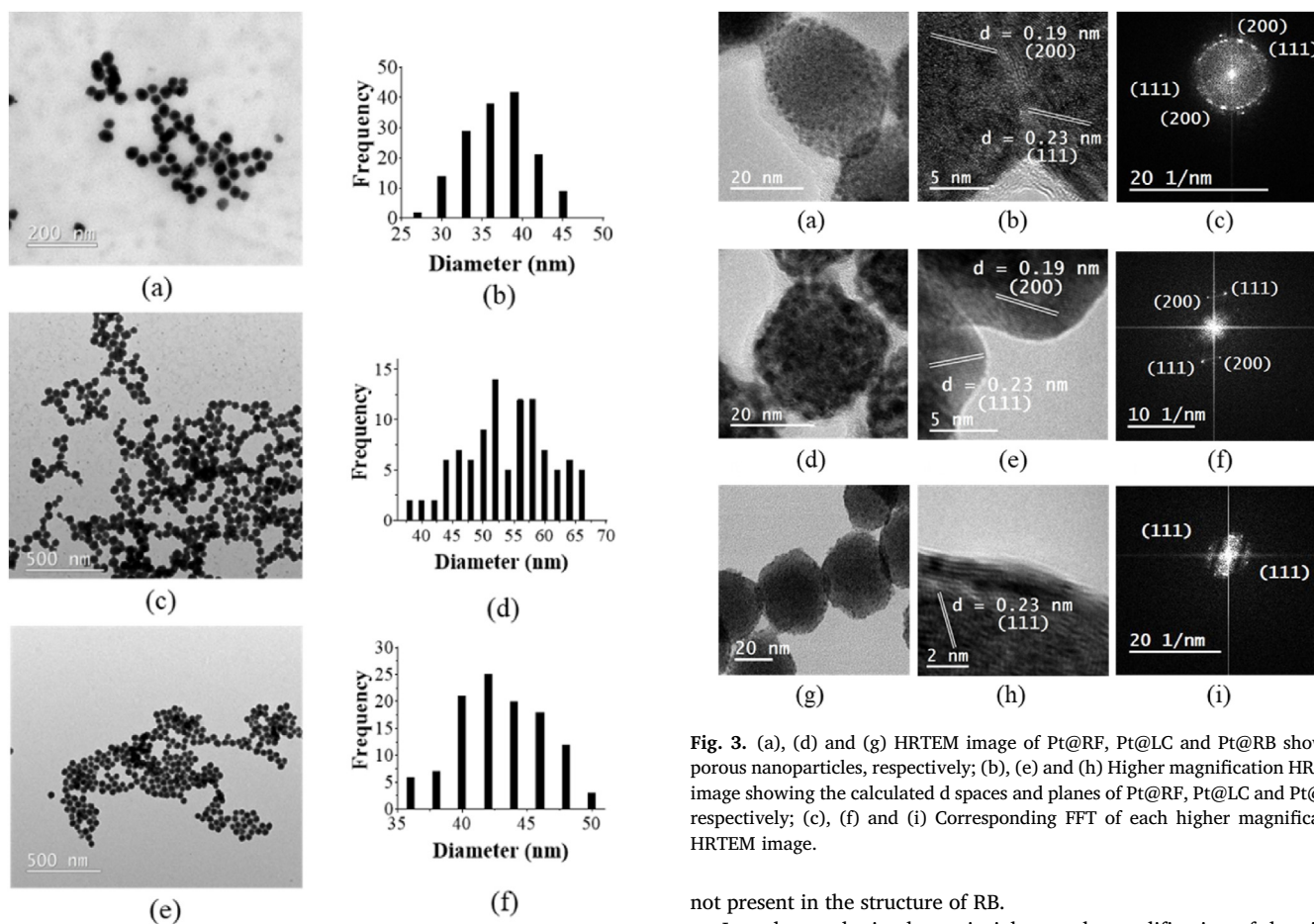

Fig. 2. Low resolution TEM image of (a) Pt@RF; (c) Pt@LC and (e) Pt@RB. Size distribution histogram of (b) Pt@RF; (d) Pt@LC and (f) Pt@RB.

Fig. 3. (a), (d) and (g) HRTEM image of Pt@RF, Pt@LC and Pt@RB showing porous nanoparticles, respectively; (b), (e) and (h) Higher magnification HRTEM image showing the calculated d spaces and planes of Pt@RF, Pt@LC and Pt@RB, respectively; (c), (f) and (i) Corresponding FFT of each higher magnification HRTEM image.

not present in the structure of RB.

In order to obtain clearer insights on the modification of the vibrational modes after the synthesis, Raman spectroscopy was performed employing a 785 nm laser excitation, to avoid any surface enhanced
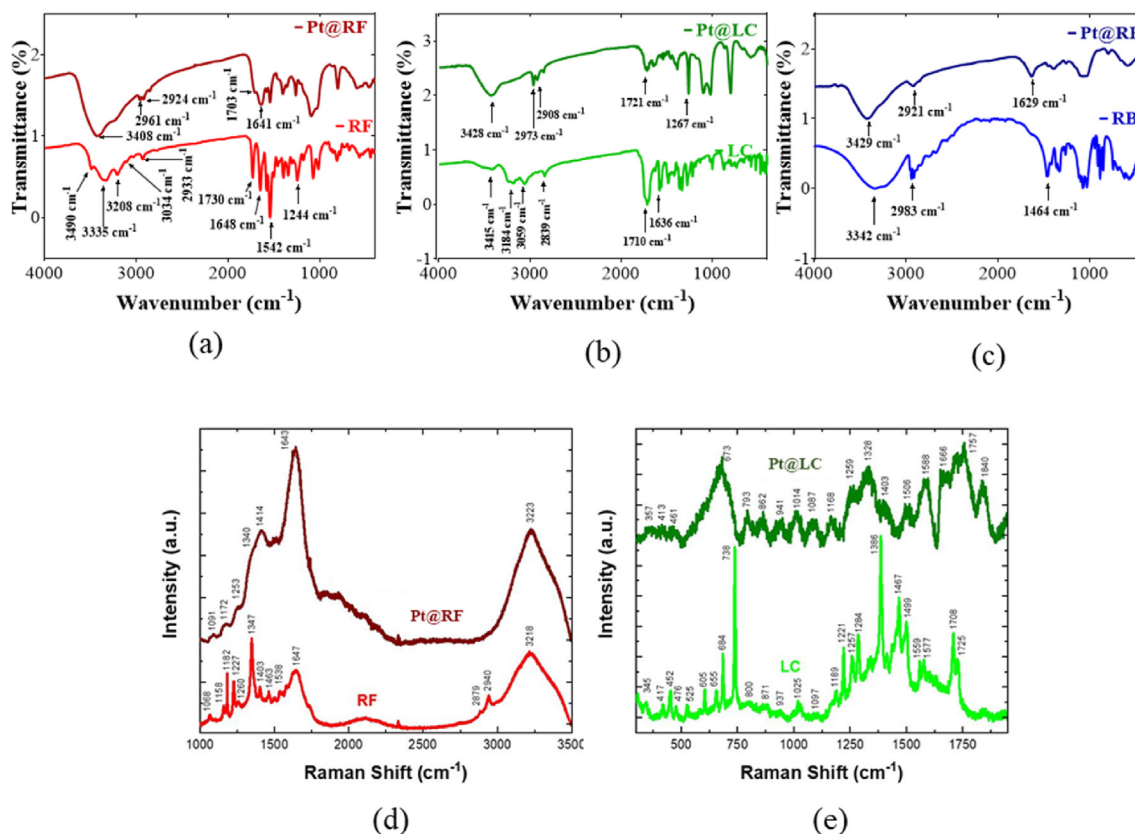
Fig. 4. (a), (b) and (c) FTIR spectra comparison between RF and Pt@RF, LC and Pt@LC and RB and Pt@RB respectively; (d) and (e) Raman spectra comparison of RF and Pt@RF and LC and Pt@LC respectively.

Raman scattering (SERS effect). In fact, the IR excitation rules out any luminescence interferences and it avoids the excitation of the surface plasmon resonance of PtNPs, that is reported at 270 nm for Pt@RF and at 263 nm for Pt@LC respectively, by UV–Vis analysis. Fig. 4 d presents the comparison of the RF solution with the Pt@RF nanoparticles. Sharp vibrational modes are observed in the Raman spectrum of RF solution at 1068, 1182, 1227, 1347, 1403, 1463, 2940 cm^{-1}. Vibrational mode assignments are assessed by comparing with previous works [52,53]. The most intense band at 1347 cm^{-1} is assigned to the C–N stretching and the C–C stretching vibration, which represents the characteristic frequency of the pyrazine ring of the molecule. Sharp and intense bands at around 1182 and 1227 cm^{-1} are ascribed to the C–N stretching mode of the uracil ring and the C–CH$_3$ stretching mode of the benzene ring. The C–H stretching-vibration modes of the benzene ring and the methyl appears at 2879 and 2940 cm^{-1}. It is worth noting the presence of two broad luminescence bands at 1643 cm^{-1} (900 nm) and at 3218 cm^{-1} (1050 nm). In the Raman spectrum of the Pt@RF, the vibrational modes appear drastically broaden and redshifted at 1091, 1172, 1253, 1340, 1414 cm^{-1}. This effect has been widely reported in previous works in SERS spectra of riboflavin stabilized nanoparticles [54]. A similar Raman analysis of RF is carried out in case of LC (Fig. 4 e). The LC solution presents a set of sharp vibrational modes between 450 up to 1750 cm^{-1}. The region around 1577 cm^{-1} is assigned to the stretching-vibration modes of the benzene-ring carbon skeleton (C–C), while the peaks at 1025, 1386, and 1467 cm^{-1} are attributed to the C–N stretching-vibration mode. The peak at 1284 cm^{-1} is related to the C–N–C in-plane bending-vibration modes in ring II and that at 738 cm^{-1} is assigned to the C–C stretching-vibration modes, while the peaks between 525 and 684 cm^{-1} are attributed to the C–N in-plane bending-vibration modes. The most intense mode at 738 cm^{-1} is attributed to the breathing mode of benzene. In the case of the Pt@LC, the Raman modes suffer of the standard broadening of the vibrational modes,

occurring due to the presence of metal nanoparticles [53].

3.2. Study of the antitumoral activity

RF antitumor properties have been reported in literature for various tumor cell lines. Muñoz et al. demonstrated the capacity of RF to induce abnormal cell morphology and a decrease in the cell proliferation rate via apoptosis in the human promyelocytic leukemia cell line HL-60 and the human epithelial cervical cancer cell line HeLa [55]. In 786-O human renal carcinoma cell line, the irradiated (using IR) RF induced cell death by apoptosis caspase-dependent, as proven by caspase 3 activation, and aggressiveness marker downregulating effects [56]. Besides, RF inhibits cell growth in androgen-independent prostate cancer (PC3), apparently dependent on the induction of caspase-mediated cell death through activation of the FasL–Fas system. Concomitantly, activity of collagen matrix-degrading proteases was reduced, suggesting anti-metastatic potential [57]. Regarding LC, Chantarawong et al. showed that it induced apoptosis in lung cancer cells via a p53-dependent mitochondrial mechanism, with a killing potency comparable to that of cisplatin [19]. Besides, potent cytotoxic activity was expressed by LC against liver (HepG2), breast (MCF-7) and colorectal (Colo-205) cancer cell lines with a IC$_{50}$ of 7.7, 15.3 and 17.6 µg/mL respectively [58]. The antitumor activity relating to RB is conflicting. RB is able to increase matriglycan in the breast cancer cell line MCF-7, but yet this enhancement is associated with neither reduced cell proliferation, nor clear alteration in cell cycle progression and the capacity of growth of the breast cancer cells [22]. Other study showed that in several human breast cancer cell lines RB significantly increases levels of antioxidants, downregulates the expression of GSH reductase and glutamate cysteine ligase (GCL) and enhances glycolysis [21]. On the other hand, it has been reported that ribitol promotes in rats' prefrontal cortex an increase in antioxidant enzymes activity (superoxide dismutase, catalase, and glutathione peroxidase),

probably secondary to enhanced production of superoxide radical [59].

We tested the antitumoral potential of our compounds, and in particular the potential of RF and LC as photosensitizers for light-activated cancer therapies, in vitro on A549 adenocarcinomic human alveolar basal epithelial cells, a well-established cell line widely used in cancer research. Firstly, cells were treated with free RF, LC and RB at increasing doses, in combination with UV-A light emitted by a Wood lamp with spectral emission centered at 375 nm, that matches well with riboflavin absorption. The dose-response histograms of the cell viability measured at 24 and 48 h, with and without 2 h UV-A irradiation, are shown in Fig. S9. The highest decrease of the viability was observed for RF treated cells (Fig. S9 top panel), where UV-A irradiation has a dramatic effect, causing a steady drop at the IC_{50} dose threshold (see the values at RF concentration 7.2 and 10 µg/mL at 24 h, or 1 and 3.5 µg/mL at 48 h). LC treated cells (Fig. S9 central panel) also showed a consistent decrease of the viability as a function of the dose and an effective inhibition activated under UV-A light (see in particular unirradiated vs irradiated graphs at 48 h). On the contrary, RB (Fig. S9 bottom panel) was found to have less effect on the cell viability, that stayed above 70 % for all the conditions, with little or no activation with light, consistently with the characteristics of the molecule that does not have fluorescence properties.

Cells were then treated with nanoparticles. In this respect, the possibility to have RF, LC and RB stabilized mesoporous PtNPs is attractive, owing to the inherent advantages of platinum for its biocompatibility and high stability. A preliminary evaluation (not shown here) of the cell viability response to PtNP, carried out by treating the cells at increasing concentrations of platinum from 0.5 to 300 µg/mL, showed that the viability was almost unaffected by the treatment. Based on these results, the highest platinum dose of 300 µg/mL was selected for further studies. Fig. 5 shows the cell viability assessed after 24 and 48 h from the administration of Pt@RF, Pt@LC and Pt@RB samples, at fixed platinum concentration (300 µg/mL). It was observed that cells treated with PtNP have nearly the same viability as the control cells and are almost unaffected by UV-A light. Cells treated with Pt@RB particles have a lower viability which is still almost unaffected by UV-A illumination. The highest antitumoral activity was observed for Pt@RF and Pt@LC. In this case, when UV-A light was applied, an enhanced response was elicited, resulting in a further significant (p < 0.05) or highly significant (p < 0.001) reduction of the cell viability. This proves that RF and LC retain their photosensitizing potential after the synthesis of platinum nanoparticles.

Additional assays were performed at 24 h on cells treated with Pt@RF, Pt@LC and Pt@RB (all at a platinum concentration of 300 µg/mL). The analysis of intracellular ATP levels (Fig. S10) showed a marked reduction in nanoparticles-treated groups with respect to control cells, consistent with the cell viability reduction. In addition, a further decrease - significant (*p < 0.05, for Pt@RF) or highly significant (**p < 0.01, for Pt@LC) - was observed as an effect of UV-A exposure. Caspase 3 activity (Fig. S11) had slightly increased but not significantly compared to the untreated control. Oxidative stress was evaluated through the analysis of intracellular levels of GSH and the quantification of enzymes with antioxidant activity, namely the expression of HO-1, SOD1 and SOD2. As reported in Fig. 6 a, a consumption of GSH, resulting in a decrease in the intracellular level at approximately 80 % compared to the control, was caused by the UV-A irradiation in presence of the nanoparticles. HO-1 and SOD2 gene expression (Fig. 6 b, d) increased significantly after UV-A irradiation of cells treated with Pt@RF and Pt@LC. However, only a slight yet not significant increase in the expression of the SOD1 gene was observed (Fig. 6c).

Finally, to strengthen all the previous findings in terms of the interaction between nanoparticles and cells, confocal microscopy imaging was carried out on cells treated with Pt@RF, where the green riboflavin fluorescence can be exploited to image spots where the Pt@RF are located. A representative set of images (red/blue/green components and the resulting merge) and a series of Z-stack images are shown in Fig. 7
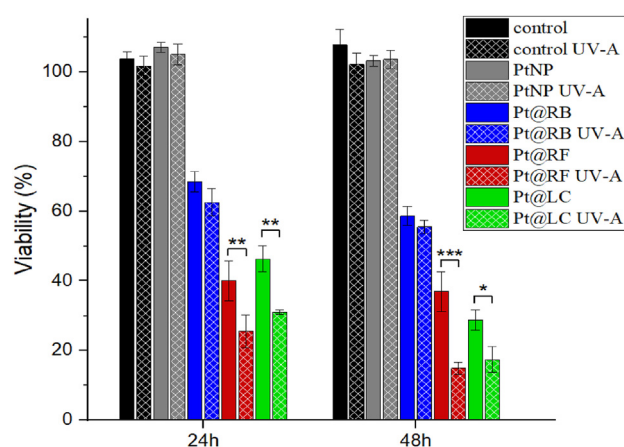

Fig. 5. Viability of A549 cells exposed to PtNP, Pt@RF, Pt@LC and Pt@RB, at the same platinum concentration (300 µg/mL), for 24 h and 48h, with and without UV-A illumination. Values are normalized to controls (%) and represent the (mean ± SD) of at least three separate experiments, each carried out in eight replicates. Significant differences: *p < 0.05; **p < 0.01; ***p < 0.001.

and Fig. S12. The red and blue fluorescence highlight the cytoskeleton of cells, labelled with the phalloidin antibody, and the cell nuclei, labelled with DAPI, respectively. The intrinsic fluorescence of the riboflavin was visible as the green spots around the cell membrane and within the cytoplasm, confirming the particles have been up-taken by cells.

Taken together, our results indicate that all the nanostructures have demonstrated a marked anti-tumor activity, highlighted by a drastic reduction in lung cancer cell viability with a significant reduction of intracellular ATP. In all cases, the effects were enhanced by UV-A irradiation. The marked anti-tumor activity of irradiated samples is expressed through the induction of oxidative stress, showed, in our study, both by the decrease in intracellular GSH and the increase in the expression of enzymes with antioxidant activity, such as HO-1 and SOD2. Confirming the literature data, the greatest effects were for Pt@LC and Pt@RF, particularly at 48 h. In our study, the anti-tumor activity of all three compounds is expressed through the induction of oxidative stress whose action presumably at various levels is capable of inducing cell death through mechanisms that will be investigated in further studies. The promising results obtained represent the starting point for the employment of mesoporous PtNPs combined with natural photosensitizers for PDT.

4. Conclusions

In summary, in this paper a one-step green approach for the synthesis of PtNP using photosensitizer RF or its related compounds LC and RB was achieved. The complete characterization of these nanostructures confirmed that mesoporous nanoparticles, with a size ranging between 30 and 60 nm, were obtained. The nanoparticles crystallinity was confirmed by HRTEM measurements, and a negative surface charge was detected by Z-potential measurements. The presence of the photosensitizer as stabilizers was confirmed by EDX analysis, FTIR and Raman spectroscopy. A marked anti-tumor activity of all nanostructures was observed, as highlighted by a drastic reduction in tumor cell viability with a significant reduction of intracellular ATP. The effects were enhanced by UV-A irradiation, notably for Pt@RF and Pt@LC that proved to be highly effective and allowed to dramatically (−70 % at 24 h, −80 % at 48 h) reduce the cell viability when illuminated by UV-A light. The samples UV triggered antitumoral activity is related to the induction of oxidative stress that leads to the decrease in intracellular GSH and the increase in the expression of enzymes with oxidative activity. These results confirm the potential of the combination of mesoporous PtNPs with natural photosensitizers for PDT treatments.
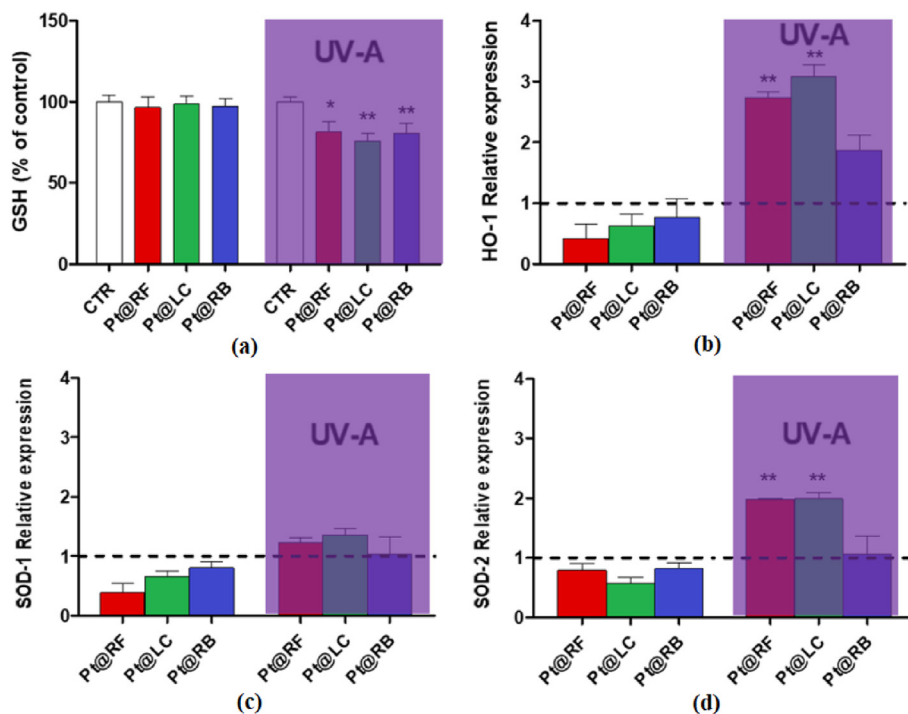
Fig. 6. GSH level (a), HO-1 (b), SOD1 (c) and SOD2 (d) expression measured after 24h in A549 cells treated with nanoparticles with and without UV-A light. In panels b, c and d, the values are normalized to controls, that is always plotted as the dashed line (y = 1). The columns represent the mean values $\pm$ SD of three separate experiments, each carried out in triplicate. Significant differences from controls: *p < 0.05; **p < 0.01.
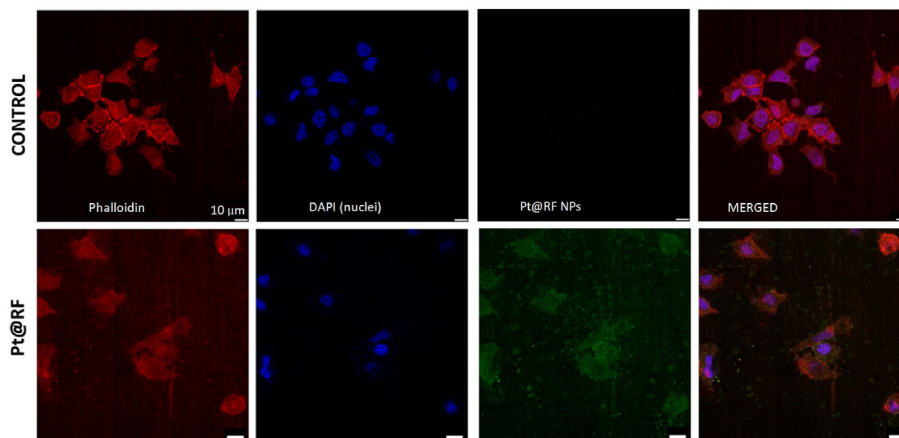

Fig. 7. Confocal images (red/blue/green components and their merge) taken on A549 cells, untreated and treated with Pt@RF at a platinum concentration of 300 μg/mL.

Declaration of competing interest

The authors declare no conflict of interest.

Appendix A. Supplementary data

Supplementary data to this article can be found online at https ://doi.org/10.1016/j.nanoms.2024.06.003.

References

[1] X. Li, J.F. Lovell, J. Yoon, X. Chen, Clinical development and potential of photothermal and photodynamic therapies for cancer, Nat. Rev. Clin. Oncol. 17 (2020) 657–674.

[2] Z. Jianhua, Z. Fuwu, F. Wenpei, L. Ling, Y. Zhen, Synthesis of novel photosensitizers for cancer theranostics, Front. Chem. 11 (2023) 1188243.

[3] D. Lee, S. Kwon, Sy Jang, E. Park, Y. Lee, H. Koo, Overcoming the obstacles of current photodynamic therapy in tumors using nanoparticles, Bioact. Mater. 8 (2022) 20–34.

[4] D. Machado, S.M. Shishido, K.C.S. Queiroz, D.N. Oliveira, A.L.C. Faria, R.R. Catharino, et al., Irradiated riboflavin diminishes the aggressiveness of melanoma in vitro and in vivo, PLoS One 8 (2013) e54269.

[5] H. Chen, K. Hou, J. Yu, L. Wang, X. Chen, Nanoparticle-based combination therapy for melanoma, Font. Oncol. 12 (2022) 928797.

[6] F. Adnane, E. El-Zayat, H.M. Fahmy, The combinational application of photodynamic therapy and nanotechnology in skin cancer treatment: a review, Tissue Cell 77 (2022) 101856.

[7] D. Dinakaran, B.C. Wilson, The use of nanomaterials in advancing photodynamic therapy (PDT) for deep-seated tumors and synergy with radiotherapy, Front. Bioeng. Biotechnol. 11 (2023) 1250804.

[8] Y. Wang, E. Chen, Interventional bronchoscopic treatment of lung cancer, Laparosc. Endosc. Surg. Sci. 5 (2022) 52–56.

[9] S. Afrasiabi, A. Partoazar, N. Chiniforush, R. Goudarzi, The potential application of natural photosensitizers used in antimicrobial photodynamic therapy against oral infections, Pharm. Times 15 (2022) 767–777.

[10] MB Rivas Aiello, F. Ghilini, JE Martínez Porcel, L. Giovanetti, P.L. Schilardi, D.O. Mártire, Riboflavin-mediated photooxidation of gold nanoparticles and its effect on the inactivation of bacteria, Langmuir 36 (2020) 8272–8281.

[11] D.H. Kingsley, S.K.C. Chang, B.A. Annous, S.D. Pillai, Evaluation of riboflavin as an enhancer for X-ray and EBeam irradiation treatment of Tulane virus, Radiat. Phys. Chem. 203 (2023) 110645.

[12] C. Wu, Y. Li, Z. Cheng, P. Wang, Z. Ma, K. Liu, et al., Cell-penetrating riboflavin conjugate for antitumor photodynamic therapy, Chin. Chem. Lett. 33 (2022) 4339–4344.

[13] MB Rivas Aiello, D. Castrogiovanni, J. Parisi, J.C. Azcárate, FS García Einschlag, T. Gensch, et al., Photodynamic therapy in HeLa cells incubated with riboflavin and pectin-coated silver nanoparticles, Photochem. Photobiol. 94 (2018) 1159–1166.

[14] I. Ahmad, Z. Anwar, S. Ahmed, M.A. Sheraz, S. Khattak, Metal ion mediated photolysis reactions of riboflavin: a kinetic study, J. Photochem. Photobiol., B 173 (2017) 231–239.

[15] I. Ahmad, Z. Anwar, S.A. Ali, K.A. Hasan, M.A. Sheraz, S. Ahmed, Ionic strength effects on the photodegradation reactions of riboflavin in aqueous solution, J. Photochem. Photobiol., B 157 (2016) 113–119.

[16] I. Ahmad, Z. Anwar, S. Ahmed, M.A. Sheraz, R. Bano, A. Hafeez, Solvent effect on the photolysis of riboflavin, AAPS PharmSciTech 16 (2015) 1122–1128.

[17] M. Sikorski, Riboflavin interactions with oxygen — a survey from the photochemical perspective, Chem. Eur J. 20 (2014) 15280–15291.

[18] H. Li, Z.Q. Jiang, Y. Pan, S.Q. Yu, Study on electron transfer of fluorescent probe lumichrome and nucleic acid by laser flash photolysis, Res. Chem. Intermed. 32 (2006) 695–708.

[19] W. Chantarawong, N. Kuncharoen, S. Tanasupawat, P. Chanvorachote, Lumichrome inhibits human lung cancer cell growth and induces apoptosis via a p53-dependent mechanism, Nutr. Cancer 71 (2019) 1390–1402.

[20] S.F. Etu, M.A. Hossain, A.S.S. Rouf, A. Alqahtani, N. Qais, Molecular docking and anticancer activity determination of 5,10-dihydro-7,8-dimethyl alloxazine derived from lumichrome of riboflavin, Main Group Chem. 20 (2021) 81–88.

[21] J.D. Tucker, R. Doddapaneni, P.J. Lu, Q.L. Lu, Ribitol alters multiple metabolic pathways of central carbon metabolism with enhanced glycolysis: a metabolomics and transcriptomics profiling of breast cancer, PLoS One 17 (2022) 1–22.

[22] P.J. Lu, J.D. Tucker, E.K. Branch, F. Guo, A.R. Blaeser, Q.L. Lu, Ribitol enhances matriglycan of α-dystroglycan in breast cancer cells without affecting cell growth, Sci. Rep. 10 (2020) 1–15.

[23] A. Abed, M. Derakhshan, M. Karimi, M. Shirazinia, M. Mahjoubin-Tehran, M. Homayonfal, et al., Platinum nanoparticles in biomedicine: preparation, anti-cancer activity, and drug delivery vehicles, Front. Pharmacol. 13 (2022) 1–23.

[24] A.A. Pawar, J. Sahoo, A. Verma, A. Lodh, J. Lakkakula, Usage of platinum nanoparticles for anticancer therapy over last decade: a review, Part. Part. Syst. Charact. 38 (2021).

[25] S.T. Yerpude, A.K. Potbhare, P. Bhilkar, A.R. Rai, R.P. Singh, A.A. Abdala, et al., Biomedical, clinical and environmental applications of platinum-based nanohybrids: an updated review, Environ. Res. 231 (2023) 116148.

[26] F. Daneshvar, F. Salehi, M. Karimi, R.D. Vais, M. Mosleh-Shirazi, N. Sattarahmady, Combined X-ray radiotherapy and laser photothermal therapy of melanoma cancer cells using dual-sensitization of platinum nanoparticles, J. Photochem. Photobiol., B 203 (2020) 111737.

[27] B. Fu, M. Dang, J. Tao, Y. Li, Y. Tang, Mesoporous platinum nanoparticle-based nanoplatforms for combined chemo-photothermal breast cancer therapy, J. Colloid Interface Sci. 570 (2020) 197–204.

[28] G. Zhu, Y. Zhao, L. Su, P. Qiu, W. Luo, Recent advances on the synthesis of mesoporous metals for electrocatalytic methanol oxidation, Emergent Mater 3 (2020) 291–306.

[29] A. López-Ruíz, E. Villaseco-Arribas, K. McEnnis, Poly(lactic-co-glycolic acid) encapsulated platinum nanoparticles for cancer treatment, Mat, Adv. 3 (2022) 2858.

[30] X. Zhu, H. Wan, H. Jia, L. Liu, J. Wang, Porous Pt nanoparticles with high near-infrared photothermal conversion efficiencies for photothermal therapy, Adv. Healthc. Mater. 5 (2016) 3165–3172.

[31] K. Shim, J. Kim, Y. Heo, B. Jiang, C. Li, M. Shahabuddin, et al., Synthesis and cytotoxicity of dendritic platinum nanoparticles with HEK-293 cells, Chem. Asian J. 12 (2017) 21–26.

[32] M. Sikder, J. Wang, G.T. Chandler, D. Berti, M. Baalousha, Synthesis, characterization, and environmental behaviors of monodispersed platinum nanoparticles, J. Colloid Interface Sci. 540 (2019) 330–341.

[33] Y. Ko, S. Krishnamurthy, Y. Yun, Facile synthesis of monodisperse Pt and Pd nanoparticles using antioxidants, J. Nanosci. Nanotechnol. 15 (2015) 412.

[34] J. Wang, X. Zhang, Z. Wang, L. Wang, W. Xing, X. Liu, One-step and rapid synthesis of "clean" and monodisperse dendritic Pt nanoparticles and their high performance toward methanol oxidation and *p*-nitrophenol reduction, Nanoscale 4 (2012) 1549.

[35] J. Ren, R.D. Tilley, Shape-controlled growth of platinum nanoparticles, Small 9 (2007) 1508–1512.

[36] S. Astanov, M.Z. Sharipov, A.R. Fayzullaev, E.N. Kurtaliev, N. Nizomov, Spectroscopic study of photo and thermal destruction of riboflavin, J. Mol. Struct. 1071 (2014) 133–138.

[37] I. Ahmad, Q. Fasihullah, A. Noor, I. Ansari, Q.N.M. Ali, Photolysis of riboflavin in aqueous solution: a kinetic study, Int. J. Pharm. 280 (2004) 199–208.

[38] M. Hosny, M. Fawzy, E.M. El-Fakharany, A.M. Omer, E.M.A. El-Monaem, R.E. Khalifa, et al., Biogenic synthesis, characterization, antimicrobial, antioxidant, antidiabetic, and catalytic applications of platinum nanoparticles synthesized from *Polygonum salicifolium* leaves, J. Environ. Chem. Eng. 10 (2022) 106806.

[39] A.S. Eltaweil, M. Fawzy, M. Hosny, E.M. Abd El-Monaem, T.M. Tamer, A.M. Omer, Green synthesis of platinum nanoparticles using *Atriplex halimus* leaves for potential antimicrobial, antioxidant, and catalytic applications, Arab. J. Chem. 15 (2022) 103517.

[40] Y. Zhang, S. Cheng, H. Jia, J. Zhou, J. Xi, J. Wang, et al., Green synthesis of platinum nanoparticles by *Nymphaea tetragona* flower extract and their skin lightning, antiaging effects, J. Arab. Chem. 16 (2023) 104391.

[41] S. Bhattacharjee, DLS and zeta potential – what they are and what they are not? J. Contr. Release 235 (2016) 337–351.

[42] B.P. Bastakoti, Y. Li, S. Guragain, S.M. Alshehri, M.J.A. Shiddiky, Z. Liu, et al., Formation of mesopores inside platinum nanospheres by using double hydrophilic block copolymers, Mater. Lett. 182 (2016) 190–193.

[43] L. Wang, C. Hu, Y. Nemoto, Y. Tateyama, Y. Yamauchi, On the role of ascorbic acid in the synthesis of single-crystal hyperbranched platinum nanostructures, Cryst. Growth Des. 10 (2010) 3455–3460.

[44] W. Yu, C. Batchelor-McAuley, Y. Wang, S. Shao, S.M. Fairclough, S.J. Haigh, et al., Characterising porosity in platinum nanoparticles, Nanoscale 11 (2019) 17791.

[45] R. Lee Penn, J.A. Soltis, Characterizing crystal growth by oriented aggregation, CrystEngComm 16 (2014) 1409–1418.

[46] H. Lee, S.E. Habas, S. Kweskin, D. Butcher, G.A. Somorjai, P. Yang, Morphological control of catalytically active platinum nanocrystals, Angew. Chem. Int. Ed. 118 (2006) 7988–7992.

[47] M.S. Refat, Synthesis, characterization, thermal and antimicrobial studies of diabetic drug models: complexes of vanadyl(II) sulfate with ascorbic acid (vitamin C), riboflavin (vitamin B2) and nicotinamide (vitamin B3), J. Mol. Struct. 969 (2010) 163–171.

[48] Y. Shuji, W. Feng, An approach to compatible multiple nonlinear vibrational spectroscopy measurements using a commercial sum frequency generation system, Analyst 136 (2011) 2489–2494.

[49] M. Wolf, C. Schumann, R. Gross, T. Domratcheva, R. Diller, Ultrafast infrared spectroscopy of riboflavin: dynamics, electronic structure, and vibrational mode analysis, J. Phys. Chem. B 112 (2008) 13424–13432.

[50] M. Takahashi, Y. Ishikawa, J. Nishizawa, H. Ito, Low-frequency vibrational modes of riboflavin and related compounds, Chem. Phys. Lett. 401 (2005) 475–482.

[51] P. Bairi, B. Roy, A.K. Nandi, Bicomponent hydrogels of lumichrome and melamine: photoluminescence property and its dependency on pH and temperature, J. Phys. Chem. B 114 (2010) 11454–11461.

[52] A. Zdaniauskienė, I. Ignatjev, T. Charkova, M. Talaiki, A. Luksa, A. Stkus, et al., Shell-isolated nanoparticle-enhanced Raman spectroscopy for probing riboflavin on graphene, Materials 15 (2022) 1636.

[53] M.J. Yun, B.S. Cheong, H.G. Cho, Surface-enhanced Raman spectroscopy and density functional theory studies of riboflavin, lumiflavin, and lumichrome adsorbed on silver colloids, Bull. Korean Chem. Soc. 40 (2019) 1183–1190.

[54] S. Chaudhuri, S. Sardar, D. Bagchi, S.S. Singha, P. Lemmens, S.K. Pal, Sensitization of an endogenous photosensitizer: electronic spectroscopy of riboflavin in the proximity of semiconductor, insulator, and metal nanoparticles, J. Phys. Chem. A 119 (2015) 4162–4169.

[55] M.A. Muñoz, A. Pacheco, M.I. Becker, E. Silva, R. Ebensperger, A.M. Garcia, et al., Different cell death mechanisms are induced by a hydrophobic flavin in human tumor cells after visible light irradiation, J. Photochem. Photobiol., B 103 (2011) 57–67.

[56] A.H. Chaves Neto, K.J. Pelizzaro-Rocha, M.N. Fernandes, C.V. Ferreira-Halder, Antitumor activity of irradiated riboflavin on human renal carcinoma cell line 786-O, Tumor Biol. 36 (2015) 595–604.

[57] K.C. de Souza Queiroz, W.F. Zambuzzi, A.C. Santos de Souza, R.A. da Silva, D. Machado, G.Z. Justo, et al., A possible anti-proliferative and anti-metastatic effect of irradiated riboflavin in solid tumours, Cancer Lett. 258 (2007) 126–134.

[58] E. Shafia Farhana, A. Ali, Q. Nazmul, 5,10-dihydro-7,8-dimethyl alloxazine as an anticancer agent from lumichrome of riboflavin, Drug Des. Dev. Ther. 2 (2021).

[59] V. Stone, K.Y. Kudo, P.M. August, T.B. Marcelino, C. Matté, Polyols accumulated in ribose-5-phosphate isomerase deficiency increase mitochondrial superoxide production and improve antioxidant defenses in rats' prefrontal cortex, Int. J. Dev. Neurosci. 37 (2014) 21–25.